

AD-A067 517

NAVAL RESEARCH LAB WASHINGTON D C
X-RAY EMISSION FROM CH₂ LASER-PRODUCED PLASMAS AT 10 TO THE 16T--ETC(U)
FEB 79 D G COLOMBANT, N K WINSOR

F/G 20/9

UNCLASSIFIED

NRL-MR-3638

SBIE-AD-E000 287

NL

1 OF 1
ADA
067517



ADE 000 287

NRL Memorandum Report 3638

5
NW

X-Ray Emission from CH₂
Laser-Produced Plasmas at 10^{16} W/cm²

D.G. COLOMBANT AND N.K. WINSOR

Plasma Theory Branch
Plasma Physics Division

LEVEL III

February 28, 1979

A067517

DDC FILE COPY



DDC
RECEIVED
APR 20 1979
B

NAVAL RESEARCH LABORATORY
Washington, D.C.

70 03 00 000

SECURITY CLASSIFICATION OF THIS PAGE (When Data Entered)

REPORT DOCUMENTATION PAGE		READ INSTRUCTIONS BEFORE COMPLETING FORM
1. REPORT NUMBER NRL Memorandum Report 3638	2. GOVT ACCESSION NO.	3. RECIPIENT'S CATALOG NUMBER
4. TITLE (and Subtitle) X-RAY EMISSION FROM CH ₂ LASER-PRODUCED PLASMAS AT 10 ¹⁶ W/cm ²	5. TYPE OF REPORT & PERIOD COVERED Interim report on a continuing NRL Problem.	
	6. PERFORMING ORG. REPORT NUMBER	
7. AUTHOR(s) D.G. Colombant and N.K. Winsor	8. CONTRACT OR GRANT NUMBER(s)	
9. PERFORMING ORGANIZATION NAME AND ADDRESS Naval Research Laboratory Washington, D.C. 20375	10. PROGRAM ELEMENT, PROJECT, TASK AREA & WORK UNIT NUMBERS NRL Problem 67H02-58 Proj. No. NP-01-05-01	
11. CONTROLLING OFFICE NAME AND ADDRESS Department of Energy Washington, D.C. 20545	12. REPORT DATE February 28 1979	
	13. NUMBER OF PAGES 33	
14. MONITORING AGENCY NAME & ADDRESS (if different from Controlling Office)	15. SECURITY CLASS. (of this report) UNCLASSIFIED	
	15a. DECLASSIFICATION/DOWNGRADING SCHEDULE	
16. DISTRIBUTION STATEMENT (of this Report) Approved for public release; distribution unlimited.		
17. DISTRIBUTION STATEMENT (of the abstract entered in Block 20, if different from Report)		
18. SUPPLEMENTARY NOTES		
19. KEY WORDS (Continue on reverse side if necessary and identify by block number) X-ray production Laser-produced plasmas Two-dimensional MHD simulation Self-generated magnetic fields <i>10 to the 16th power W/sq cm</i>		
20. ABSTRACT (Continue on reverse side if necessary and identify by block number) → X-ray spectra from CH ₂ laser-generated at 10 ¹⁶ W/cm ² are compared with those obtained using a 2D-mhd code. Good agreement is found over 7 orders of magnitude for X-ray energies comprised between 1 and 300 keV. It is found that the hard X-ray spectrum is compatible with the generation of B-fields in the interaction region. Variation of the numerical results with initial conditions, ion mass, laser energy deposition and grid size is investigated. R		

DD FORM 1473
1 JAN 73

EDITION OF 1 NOV 65 IS OBSOLETE
S/N 0102-014-6601

SECURITY CLASSIFICATION OF THIS PAGE (When Data Entered)

79 03 09 022

CONTENTS

INTRODUCTION	1
MODEL	2
STANDARD CASE	3
RESULTS	7
CONCLUSIONS	10
ACKNOWLEDGMENTS	10
REFERENCES	10

ACCESSION for	
NTIS	White Section <input checked="" type="checkbox"/>
DDC	Buff Section <input type="checkbox"/>
UNANNOUNCED	<input type="checkbox"/>
JUSTIFICATION _____	
BY _____	
DISTRIBUTION/AVAILABILITY CODES	
Dist.	MAIL or SPECIAL
A	

X-RAY EMISSION FROM CH₂ LASER-PRODUCED PLASMAS AT 10¹⁶ W/cm²

INTRODUCTION

Experimental X-ray spectra have been used to demonstrate the existence of suprathermal electrons¹, ion acoustic turbulence² and self-generated magnetic fields³. The first two phenomena imply nonthermal electron distribution functions whereas the third one results in the production of energetic thermal electrons. Davis and Rogerson⁴ have shown that it is quite difficult to distinguish between these different types of electron distribution functions from Bremsstrahlung measurements, the main difference being at high photon energies where statistical measurement errors are usually large.

Since the experimental data does not exclude the magnetic field interpretation, we look further into it. We present more details of the physical model and show where the different components of the X-ray spectra originate. We illustrate the dependence of the computed spectra on different physical parameters. We present the dynamics a two-dimensional numerical model predicts for a laser-slab target interaction. We finally include tests of X-ray spectra sensitivity to parameters such as grid size, flux-limiting factors and different laser absorption mechanisms.

MODEL

The basic model has been described previously³. Some of its unique features are that it uses an equation of state⁵ rather than an ideal gas law to describe the plasma produced, it provides a complete treatment of magnetic field effects, including the tensor thermal conductivity. Also, the 2-dimensional code does not contain any adjustable parameters.

In addition to the features mentioned in Ref. [3], a simple form for radiation pressure⁶ has been included in the momentum equation and a more complete thermal conductivity tensor has been included. In particular, the Peltier heat conduction term $q = \beta \cdot u$ has been added where u is the electron drift velocity and β is given by

$$\beta_{11} = N_e T_e \beta_0$$

$$\beta_{\perp} = \frac{N_e T_e (\beta_1' x_0^2 + \beta_0')}{(x_0^4 + \delta_1 x_0^2 + \delta_0)}$$

where the β 's and $x = \omega\tau$ are defined in ref. 7. The cross-conductivity in the Fourier heat conduction term

$$K \hat{b} \times \nabla T_e \text{ with } K = \frac{Z N k T_e \tau_{ei}}{m} \frac{x_0 (\gamma_{1..} x_0^2 + \gamma_0'')}{(x_0^4 + \delta_1 x_0^2 + \delta_0)}$$

has also been included. We wish to emphasize the fact that we use the classical conductivity and do not flux-limit our transport. As we show below, results with and without flux-limiting are nearly identical. This may be interpreted as a demonstration that our fluid model is self-consistent. Should the flux-limited and non-flux-limited results be significantly different, then the hypotheses on which the fluid model was derived would be violated.

The equation for the magnetic field as reported in this work does not contain the thermal force whose effects are reported in detail in ref. 8. The spectral results reported here are obtained with free-free X-ray diagnostics which have been added to the code by breaking the

bremsstrahlung radiation rate into 17 frequency intervals:

$$P_{brem}(E_1, E_2) = P_{bl} e^{-(E_2 - E_1)/kT_l}$$

Here P_{bl} and T_l are the local total bremsstrahlung radiation rate and temperature obtained from the local ion and energy densities through the equation of state. The frequency intervals were chosen to correspond to the range of experimental interest and the radiation output in each frequency range was integrated over space and time to obtain the total output. For the X-ray energies considered, it was assumed that half the radiation escaped from the plasma into 2π steradians, and the remaining half was deposited in the solid region.

STANDARD CASE

All of the results which are presented in this section correspond to the following input parameters: 1.2 J of 1.06 μ light deposited in a 12 μ radial focal spot in a pulse with a FWHM of 20 psec. The pulse is Gaussian in space and time and has a peak flux of $1.2 \cdot 10^{16}$ W/cm². No prepulse precedes the main pulse. The target is a plane polyethylene slab - and a steep gradient density has been set up in front of it in order to start the calculations. Figure 1 depicts the initial laser and target conditions. The laser parameters are typical of the experiments performed with the NRL laser facility³.

In the following, we present in detail the numerical results obtained with the model described in the previous section on a 12 μ by 12 μ grid. Then, we investigate different physical effects such as variation of the initial density gradient, the ion atomic mass, the absorption coefficient and of the inclusion of a flux-limiter. Finally we present partial results obtained for the same physical case with a 4 μ by 4 μ grid.

Figure 2 schematically pictures the target density and temperature profiles and illustrates some features of these profiles which will be used to explain the magnetic field dynamics

below. Figures 3 through 5 are profiles of fluid variables along the axis for selected times near peak intensity and later in the pulse (from 2 to 72 psec after the peak of the laser pulse). In these figures, the maximum in temperature occurs near the critical surface (where the absorption is maximum) and it follows rather closely the laser power variation with time. It reaches 60 keV 2 psec after the peak of the laser pulse and drops to about 1 keV 72 psec after that peak. Note that at $t = 21$ psec after the pulse maximum, a series of maxima appears in the temperature profile. These maxima might be an indication of an acoustic instability driven by the magnetic source terms.

The density profile has been reshaped by the laser pulse by the time of the peak of the laser pulse and shows a very large gradient in the vicinity of the critical surface. The density jumps by a factor of 50 to 100 over two cells or 24μ . This sharp gradient is moving inwards into the target whereas a rarefaction shock propagates outwards, towards the laser beam. This feature might suggest that a steady-state density gradient forms rapidly near the critical surface and that the experimental results are thus very weakly dependent on the presence of a prepulse. This feature also explains the weak dependence of the numerical results with the values of the initial density gradient. We remark here that special numerical techniques⁹ are used here which accurately preserve the physics of such shock processes¹⁰.

The self-generated B-field is also shown in those figures (off-axis at $r = 12\mu$) and we see that its maximum value (when the thermal force is not included) remains almost constant at over 2 MG for the first 88 psec. This magnetic field is a dominant feature of the interaction region and once generated, diffuses both into the target and towards the laser. The maximum B-field occurs near the critical surface and field reversals increase with time. We recall that these field reversals diminish with the addition of the thermal force term⁸.

The complicated B-field profile results from the structure of the density and temperature

gradients. Note however that the dominant term is $\partial n / \partial z \partial T / \partial r$. The positive radial density gradient term due to the presence of the initial density gradient gives a much smaller contribution to the field source term ($\partial n / \partial r \partial T / \partial z$) and thus shows that the initial density gradients only perturbs slightly the solution. The maximum value of the B-field remains at a high level during the laser pulse, because as we have seen, $\partial n / \partial z$ is approximately constant during the laser interaction as well as $\partial T / \partial r$ which remains also constant due to the reduced conductivity. It is also apparent from Fig. 5 that the B-field is carried off with the plasma as the gradients in the expanding shock move away.

The parameter $\omega_{ce} \tau_{ei}$ is a measure of the reduction in the perpendicular thermal conduction. Its peak follows the maximum in magnetic field and reaches a value greater than 10^3 . The consequent reduction in heat conduction at that time varies from a factor of 10^3 for the cross-conductivity to 10^6 for the perpendicular one. It is this reduction in heat conduction which accounts for the high temperatures observed numerically and for the hard X-rays which are also observed experimentally.

The total radiation power output peaks just behind the critical surface where the density is large and the temperature still above a few hundreds of eV. At early times, a strong emitting region is also seen associated with the outward moving shock, but as the shock wave moves to lower densities and cools by expansion, this strongly emitting region disappears. The maximum radiated power region is shown as a function of time in Fig. 6. At first it occurs inside the spike the laser beam forms inside the target. Then it spreads outwards to reappear on the axis. This pattern can be explained in terms of diffusion and fluid motion. The heat is carried radially by convection and conduction, taking the emitting region with it but when the density drops too low, the maximum emitting region reappears on the axis.

Fig. 7 to 12 show temperature and velocity contours for various times. Velocities are

directed at first toward the laser beam and then spread out radially. Also the front of the expansion accelerates from 4×10^7 cm/sec at $t = 18$ psec to 10^8 cm/sec at $t = 88.5$ psec which correspond to average ion energies going from 7.7 keV to 48.4 keV.

Before interpreting the spatially time-integrated X-ray spectra, we have plotted the X-ray power emitted between 1 and 5 keV and above 5 keV in Fig. 13. We see that the maximum of the harder X-rays comes earlier, around 30 psec after the beginning of the interaction when the laser pulse is still on. This indicates clearly that the hard X-rays are due to the high temperatures generated in the plasma near the peak of the laser pulse. Lower energy X-rays come later when the temperature drops due to the decrease in laser power and to heat diffusion. Recently, these time-resolved X-ray spectra have just been obtained experimentally¹¹ and should provide the basis for a more detailed comparison than that one provided below.

The spatially and time integrated X-ray spectrum is shown in Fig. 14 along with the experimental spectrum obtained at NRL³. By comparison, a spectrum obtained with the magnetic field artificially set to 0 is also shown. The hard X-rays have been already explained in terms of the high temperatures (tens of keV) generated during the laser interaction. However, these calculated intensities are larger than the measured ones. Although the inclusion of the thermal force terms reduce the X-ray intensities, other reasons can be given to explain the larger X-ray intensities found numerically. We shall mention two reasons here. (1) Electrons of 100 keV for example have a Larmor radius of 8μ in a 1 MG B-field, which is comparable with the size of the high B-field region. Thus, the electrons would see an inhomogeneous magnetic field and drift out of the hot region. (2) Another fact is that for $T_e = 40$ keV and $n_e = 10^{21}$ cm⁻³, the electron self-collision time is 400 psec which is much larger than the characteristic times in the experiment. So, although electrons might be produced at 40 keV, they do not maxwellize on the time scales of the experiment and as a result, they contribute to an overestimated hard X-ray contribution. This very hard part of the spectrum is also that one where

NRL MEMORANDUM REPORT 3638

the experimental uncertainty is the largest since the number of photons in this range is orders of magnitude below than in lower energy ranges.

The soft component of our calculated X-ray spectrum is much more difficult to compare accurately with experiment because sharp gradients in both densities and temperature occur over 1 or 2 cells. The resolution is poor for that region of the laser target interaction and it will be seen later how this part of the spectrum varies with the grid size. In any case, the agreement is reasonably good for energies above 1 keV which correspond to temperatures just on the border of that sharp gradient region. One feature of the experimental X-ray spectrum does not show in the numerical curve; it is the dip in the spectrum between 2 and 10 keV. This dip seems to indicate a decoupling mechanism between low energy electrons and higher energy electrons. In particular, the higher energy electrons might not be suited for a temperature representation (since they do not have time to maxwellize) and they would not obey either a diffusion equation. These remarks do not reflect on the origin of suprathermal electrons but suggest that once suprathermal have been identified in the physical interaction, their transport might have to be done differently.

When the magnetic fields are artificially set to 0, the hard X-ray component of the spectrum disappears almost completely since for $h\nu = 40$ keV, the X-ray intensity is 4 orders of magnitude smaller. This constitutes strong evidence for the role played by large B-fields in producing the high temperatures needed to explain the hard X-ray experimental data.

RESULTS

We now discuss specific conclusions obtained from comparisons of calculations with this model, and their dependences on physically interesting parameters. We consider the influence of the initial density gradient, the ion mass, the laser absorption mechanism, the importance of fine structure, and the presence of flux-limiting.

As mentioned previously, the initial density gradient is not playing a significant role in the value of the integrated X-ray spectrum. Results shown in Fig. 15 with density gradient length varying from 20μ to 41μ illustrates this result since the variation in X-ray intensity is a factor of 2.5 at most. The above variations in density gradient lengths correspond to a dip in densities varying by 4 orders of magnitude over the distance comprised between the boundary and the critical surface. This result reinforces the conclusion that the laser light produces its own density profile in the interaction region and that the X-ray spectrum is insensitive to the presence of a prepulse. The density structure near the critical surface might also explain some features of backscattered light.

The model which we have used to describe the laser target interaction is a one fluid model whereas two ion species make up the target material: carbon and hydrogen. Leaving aside the question of ion separation and acceleration, computations were made with carbon or polyethylene mass for the ions. The resulting spatially-and time-integrated X-ray spectra are shown in Fig. 16. These two curves are very similar since a factor of at most 3 separates the X-ray intensities over the entire X-ray energy range. In view of the similarity of these results and because the polyethylene case was much longer to run than the carbon case (since the velocities are larger for lighter ions and as a consequence, the time step is much smaller), all other cases shown were run with the carbon ion mass.

Absorption by an evanescent wave in the overdense region was also considered as an alternate energy deposition mechanism. An arbitrary fraction (50%) of the energy reaching the critical surface was assumed to go into the evanescent wave. Since more energy gets behind the critical surface and less energy heats the critical surface, the maximum temperature is expected to be lower than for the standard case but higher in the overdense region. This should lead to a loss of intensity for hard X-rays and increase in intensity for soft X-rays. Figure 17 shows these trends where variations are at most a factor of 4.

NRL MEMORANDUM REPORT 3638

The most severe limitation on the results presented here is undoubtedly the spatial resolution in the vicinity of the critical surface where large gradients occur. A limited attempt was made at assessing the influence of the grid size on the solution. A run was performed up to the time of the peak of the laser pulse with a $4\mu \times 4\mu$ grid instead of the $12\mu \times 12\mu$ grid used in the standard case. Profiles for density, temperature, B-field show more structure at the same time and the integrated X-ray spectra is shown in Fig. 18. This spectrum shows a difference of a factor of 2 in the hard X-ray region and an increase by a factor of 2 in the soft X-ray range. This increase confirms the need for a more detailed solution in regions of large steep gradients.

In conclusion, although the details of the interaction might change slightly due to the spatial resolution, the integrated X-ray spectra which reflect gross features like maximum temperature obtained and extent of heated regions agree reasonably well and do not raise questions about different phenomena taking place as a result of the interaction.

Because of large gradients in temperature, the thermal flux may become larger than $1/2 n_e m_e v_{the}^3$. Runs with and without flux limiter were performed and results appear in Figs. 19 and 20. In Fig. 19, electron temperature profile on the axis at the peak of the laser pulse is shown for the cases $B = 0$ and $B \neq 0$, with and without flux limiter. It is seen that the difference between the cases with and without flux-limiter is relatively small. The corresponding X-ray spectra are shown in the following figure. The higher intensities for the hard X-ray follow from the higher temperatures observed in the previous figure. The effect of the flux-limiter is very small on our results and indicates that the calculations are performed well within the limits of fluid theory.

CONCLUSION

We have found good agreement between numerical and experimental X-ray spectra for experimentally-measured plasma parameters, during the interaction when a CH_2 target is irradiated by 10^{16} W/cm^2 of 1.06 light. We have shown that this agreement is preserved when initial conditions, ion mass, laser energy deposition and grid size are changed but not when the self-generated B-fields inside the laser-produced plasma was artificially set to 0. These results, supplemented by results in ref. 8, indicate that B-fields which have been measured directly and indirectly represent one of the most probable explanations for the observation of the hard X-ray spectrum.

We have shown also that the hard X-ray pulse follows very closely the laser pulse in time, a fact which could be checked eventually in an experiment. We have also shown that a more accurate prediction of soft X-rays requires improved resolution in the region of steep gradients. We draw attention to the small influence played by a flux-limiter in our calculations. Finally, we observe that oscillations in the temperature profiles could come from an acoustic instability driven by the magnetic source terms.

ACKNOWLEDGMENTS

This work is supported by Department of Energy contract ES-77-A-01-6021.

REFERENCES

1. V.W. Slivinsky, H.N. Kornblum and H.D. Shay, J. Appl. Phys., **46**, 1973 (1975)
2. R.C. Malone, R.L. McCrory and R.L. Morse, Phys. Rev. Lett. **34**, 721 (1975)
3. B.H. Ripin, P.G. Burkhalter, F.C. Young, J.M. McMahon, D.G. Colombant, S.E. Bodner, R.R. Whitlock, D.J. Nagel, D.J. Johnson, N.K. Winsor, C.M. Dozier, R.D. Bleach, J.A. Stamper and E.A. McLean, Phys. Rev. Lett. **34**, 1313 (1975)

NRL MEMORANDUM REPORT 3638

4. J. Davis and J.E. Rogerson, *Solar Phys.* **51**, 185 (1977)
5. D. Mosher, *Phys. Rev. A*, **10**, 2330 (1974)
6. D.G. Colombant, K.G. Whitney, D.A. Tidman, N.K. Winsor and J. Davis, *Phys. fluids*, **18**, 1687 (1975)
7. S.I. Braginskii, in *Reviews of Plasma Physics*, edited by M.A. Leontovich (Consultants Bureau, New York, 1965), p. 205.
8. D.G. Colombant and N.K. Winsor, *Phys. Rev. Lett.* **38**, 697 (1977)
9. J.P. Boris and D.L. Book, *J. Comp. Phys.* **11**, 38 (1973)
10. D.G. Colombant and J.H. Gardner, *J. Comp. Phys.* **22**, 389 (1976)
11. H.G. Ahlstrom, *Bull. Amer. Phys. Soc.* **22**, 1089 (1977)

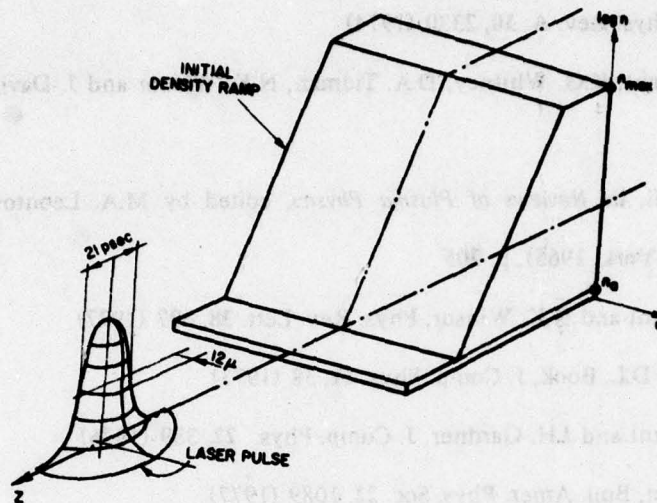


Fig. 1 — Initial density profile and laser pulse used in numerical calculations. The ratio n_0/n_{\max} will be varied and results reported in Fig. 15.

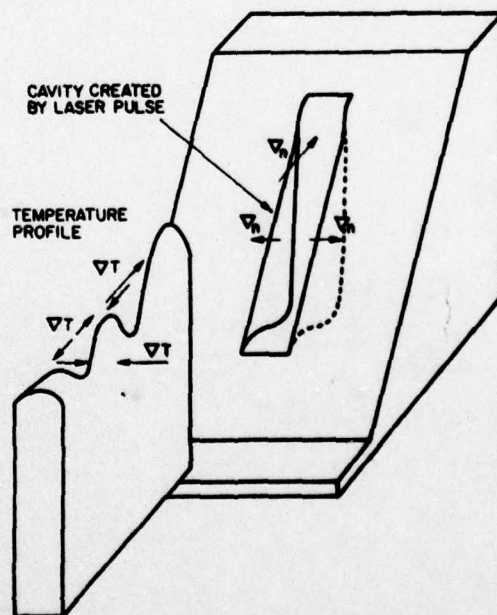


Fig. 2 — Typical density and temperature profiles near the peak of the laser pulse. Note radial ∇n due to initial conditions of Fig. 1.

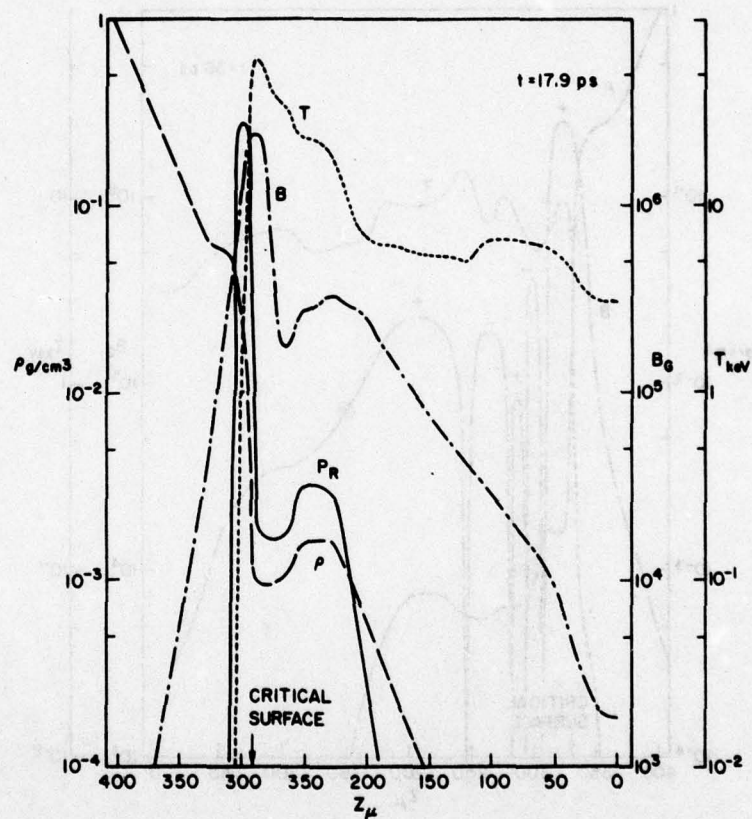


Fig. 3 — Temperature, density, B-field and radiated power profiles along the axis at $t = 17.9$ psec (2 psec after the peak of the laser pulse). B-field profiles are shown at $r = 12\mu$.

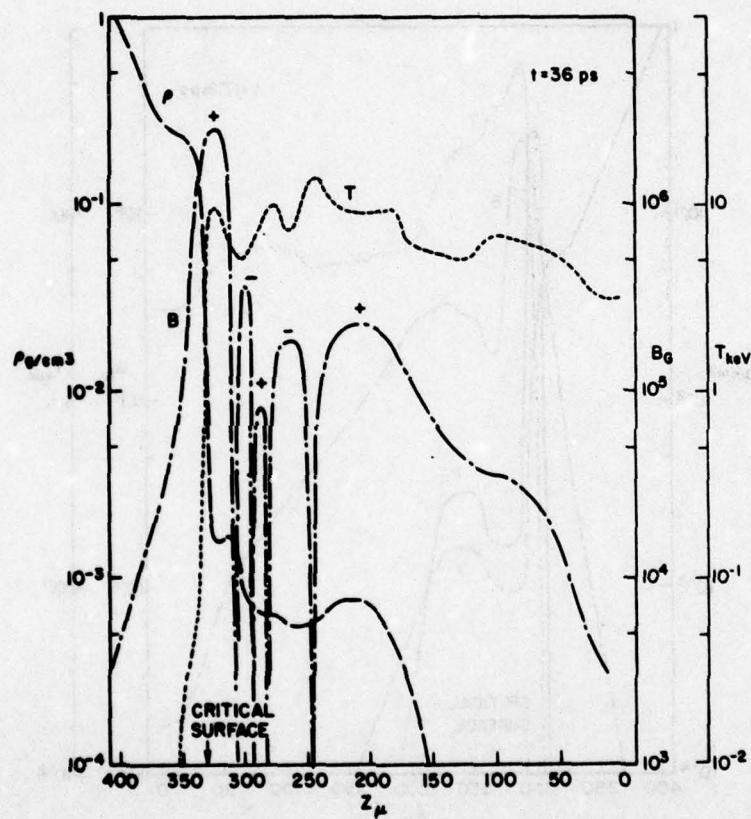


Fig. 4 — Same profiles at $t = 36$ psec + and - indicate sign of B field.

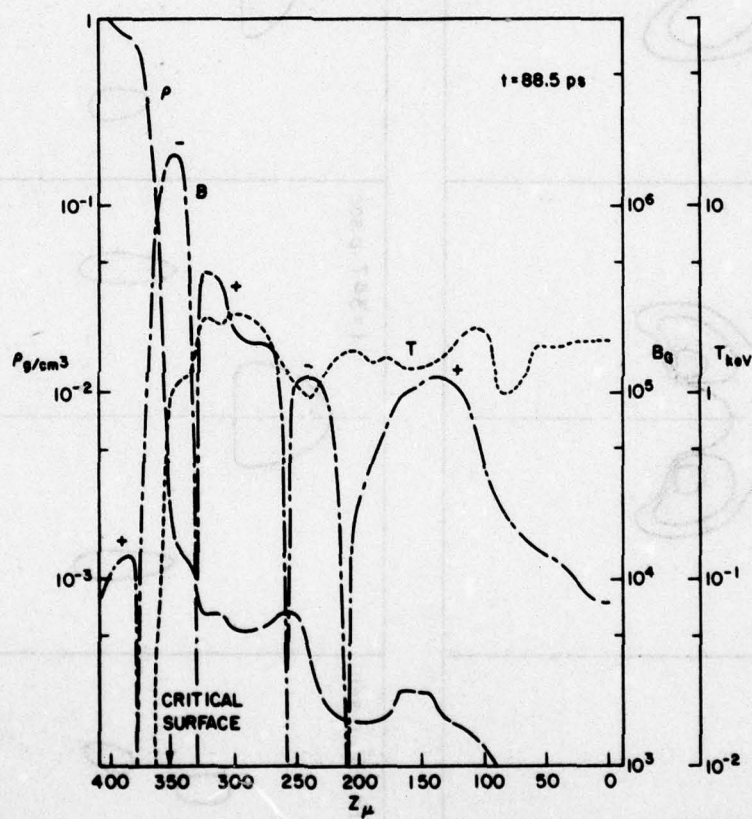


Fig. 5 - Same profiles as in Fig. 3 at $t = 88.5 \text{ psec}$.

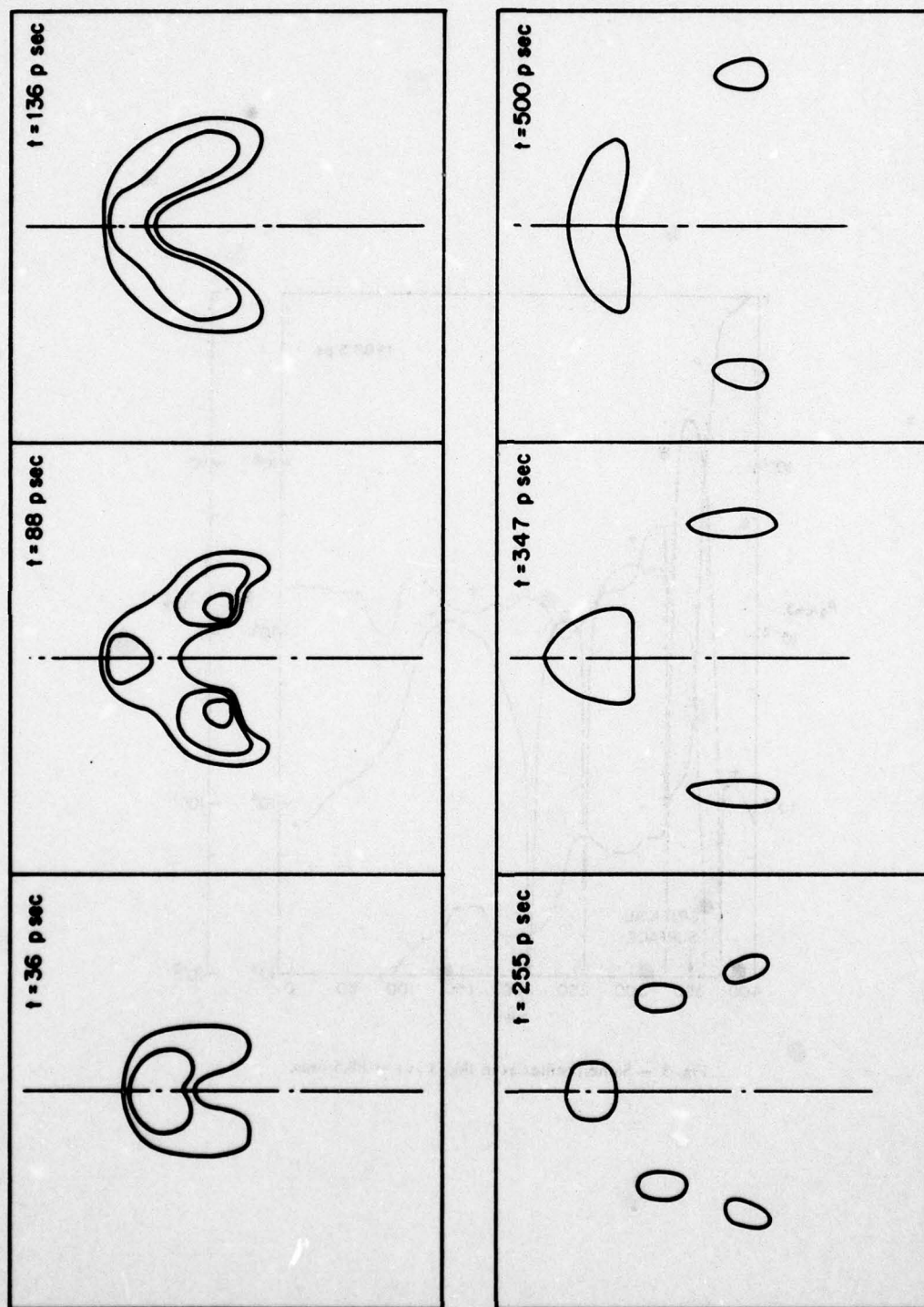


Fig. 6 — Schematic of the radiation contour intensities at various times during the interaction.

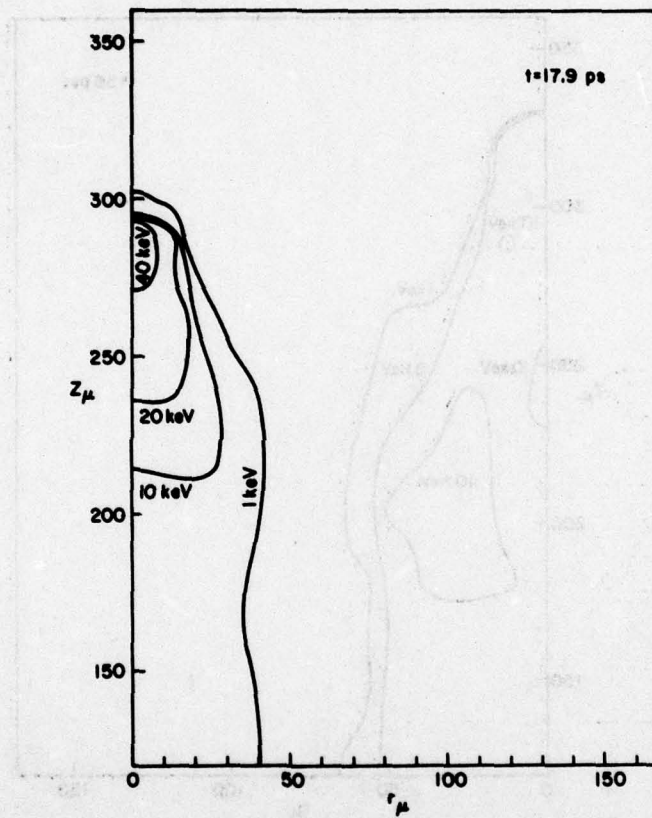


Fig. 7 - Temperature contours at $t = 17.9$ psec

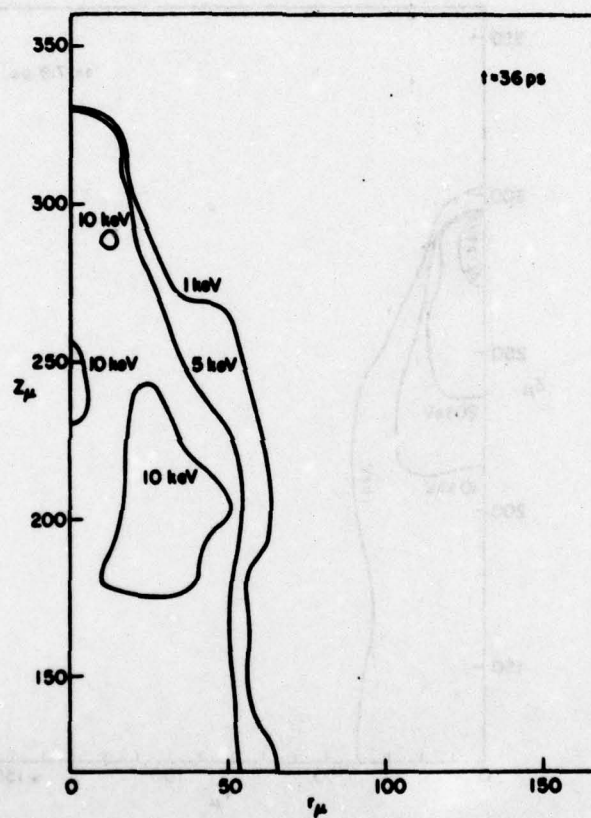


Fig. 8 - Temperature contours at $t = 36$ psec

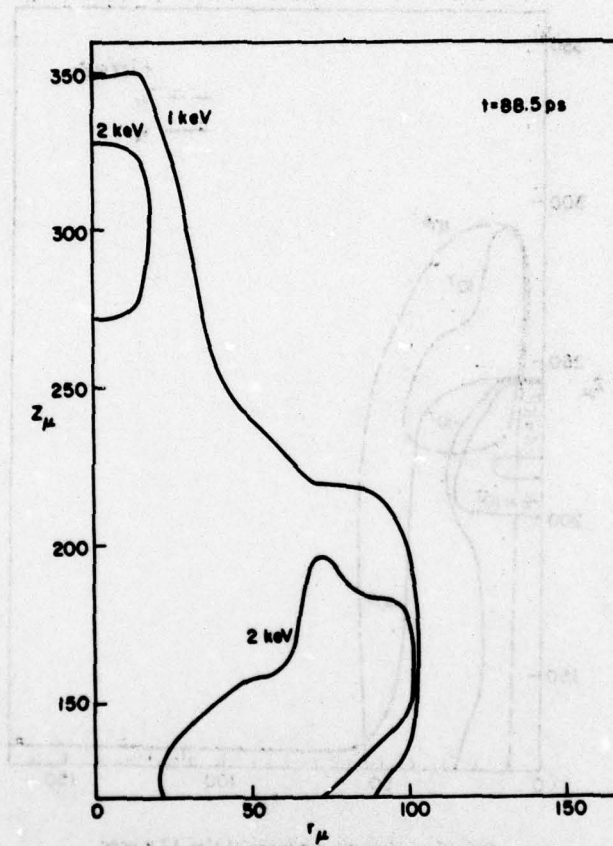


Fig. 9 — Temperature contours at $t = 88.5$ psec

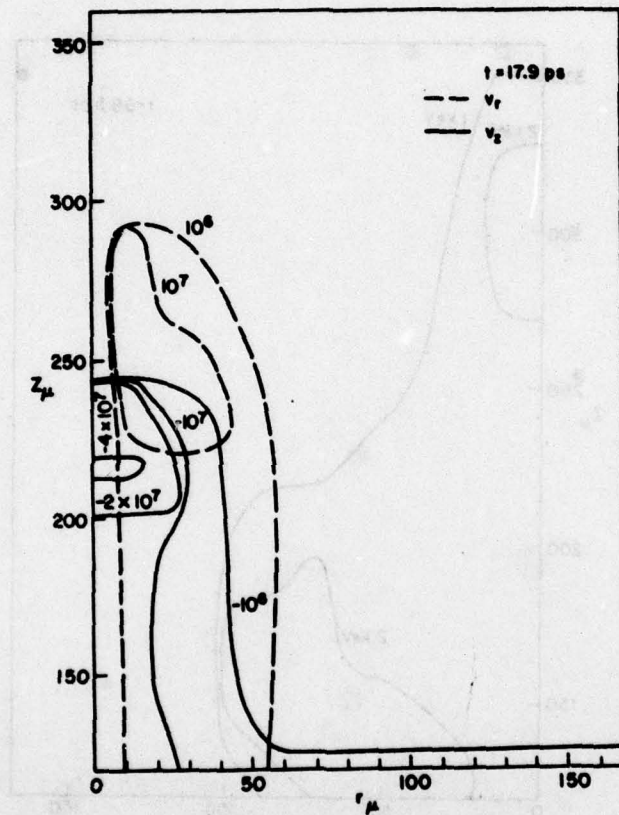


Fig. 10 — Velocity contours at $t = 17.9 \text{ ps}$

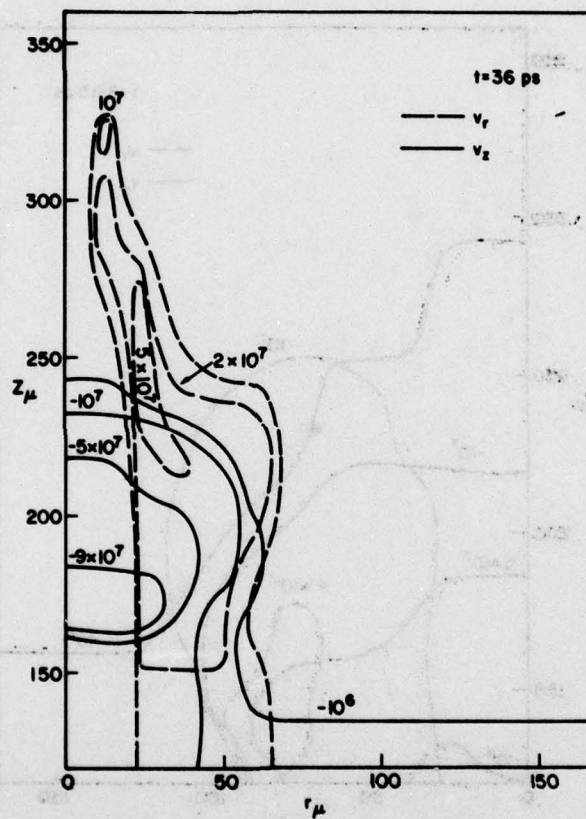


Fig. 11 — Velocity contours at $t = 36 \text{ psec}$

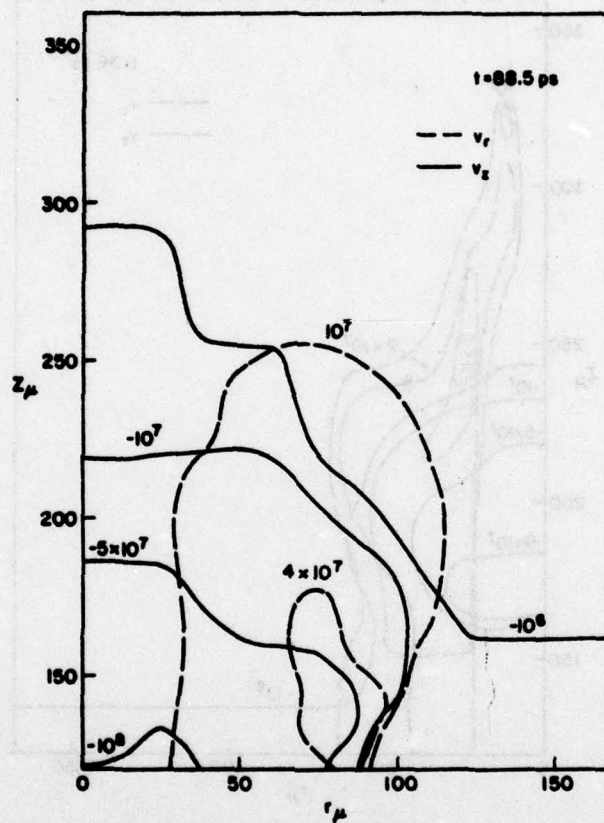


Fig. 12 — Velocity contours at $t = 88.5 \text{ ps}$

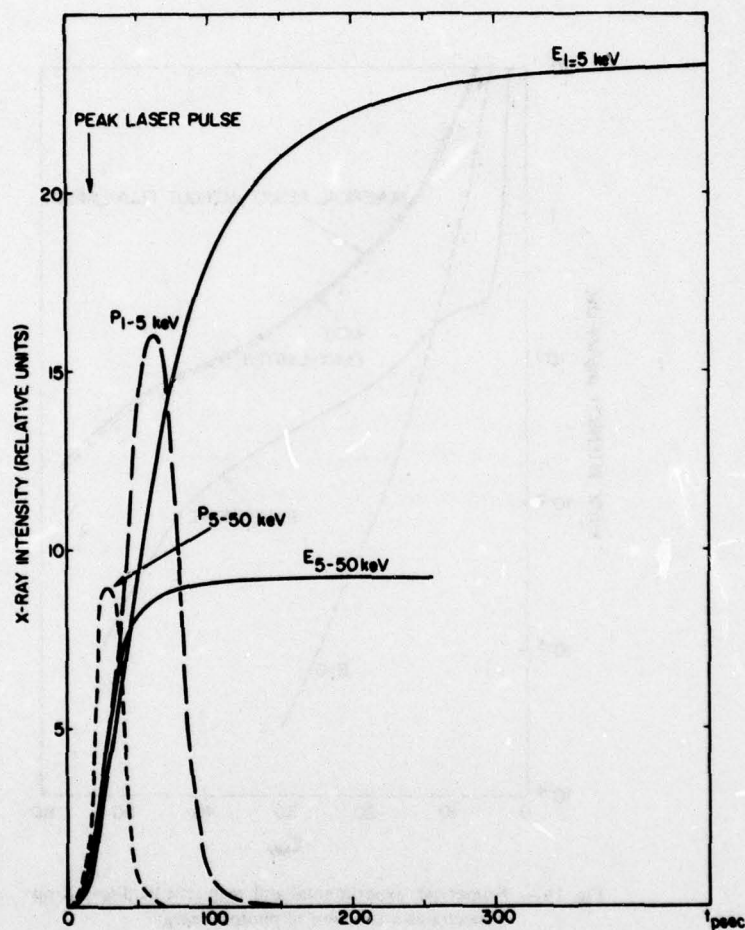


Fig. 13 — Radiated powers and energies for two photon energy bins as a function of time. Scale is not the same for the two photon energy bins.

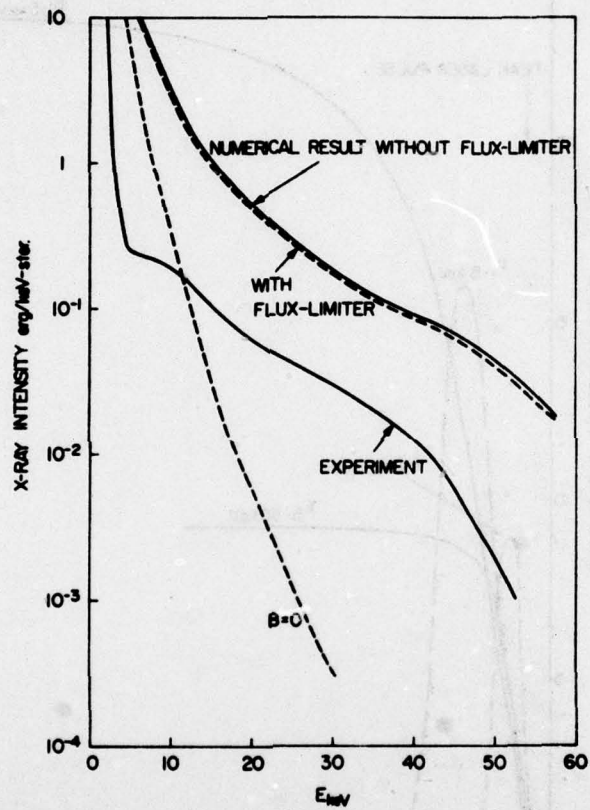


Fig. 14 — Numerical, experimental and magnetic field-less X-ray spectra as a function of photon energy.

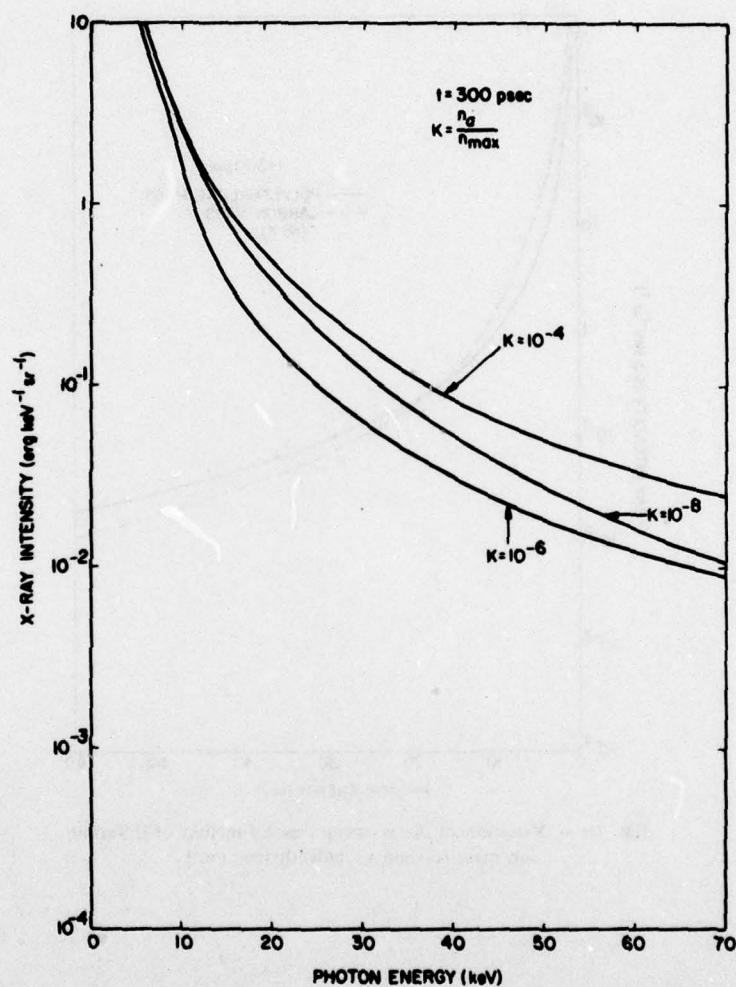


Fig. 15 — Variation of X-ray spectra at $t = 300 \text{ psec}$ as a function of the ratio n_0/n_{\max} (see Fig. 1) — "Standard" case corresponds to $K = 10^{-4}$.

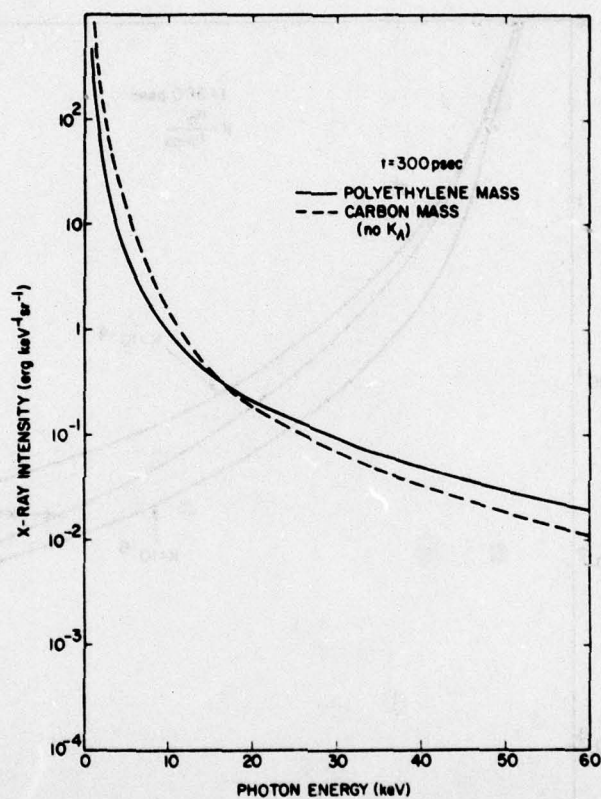


Fig. 16 — Variation of X-ray spectra as a function of different ion mass (carbon vs. polyethylene ion.)

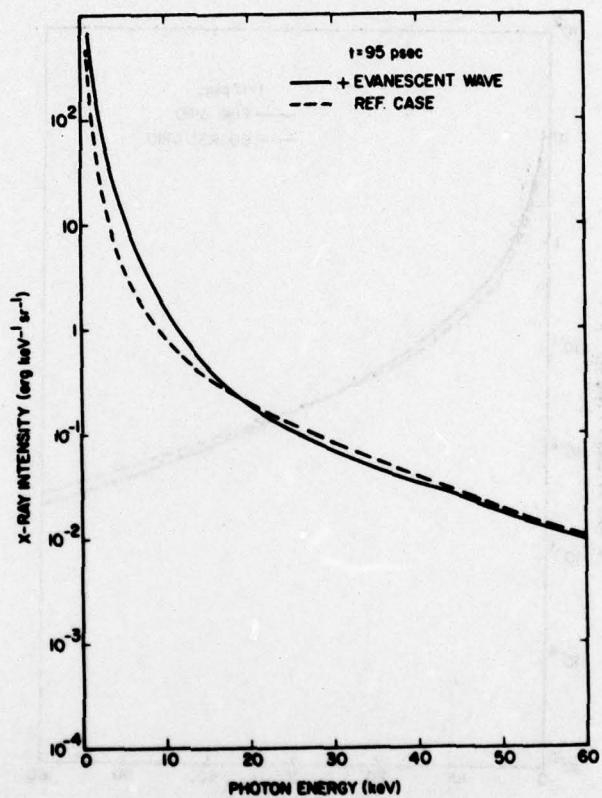


Fig. 17 — Influence of different absorption mechanism on the X-ray spectra.

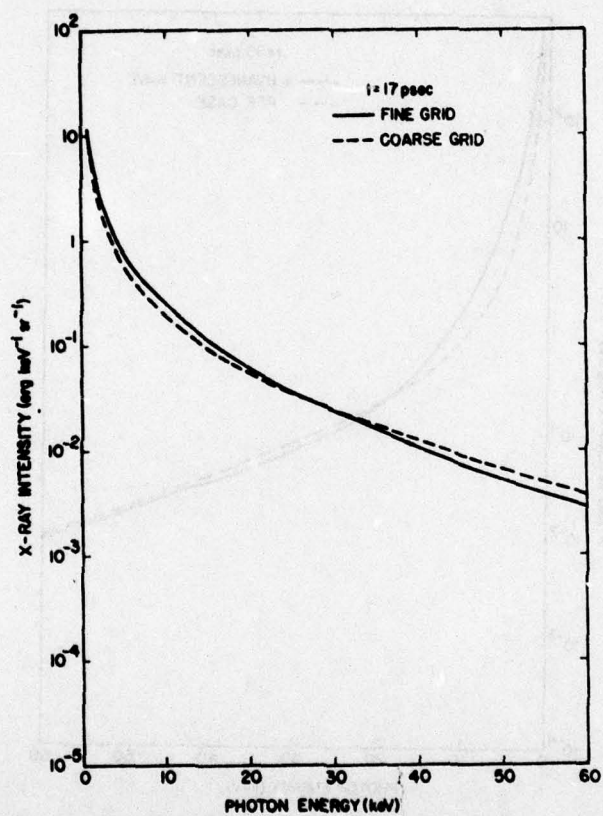


Fig. 18 — Influence of different grid size on the X-ray spectra. The fine grid calculation was carried in time up to 17 psec only (corresponding to the peak of the laser pulse)

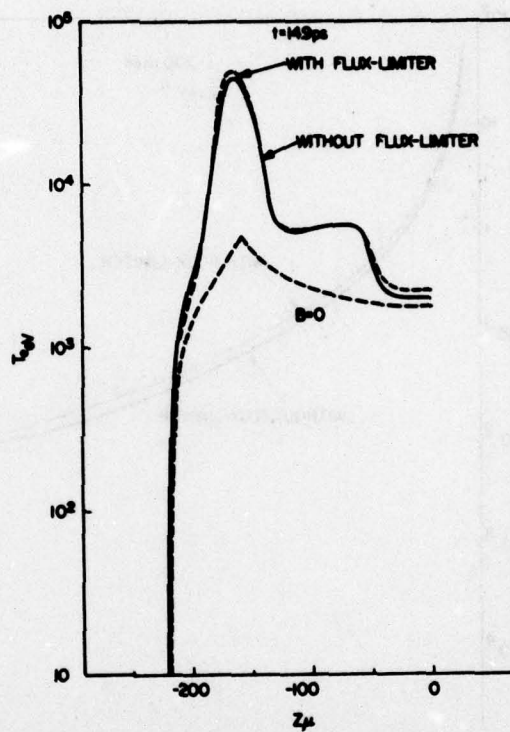


Fig. 19 — Influence of flux-limiter and $B = 0$ on the temperature profile on axis at $t = 15$ psec

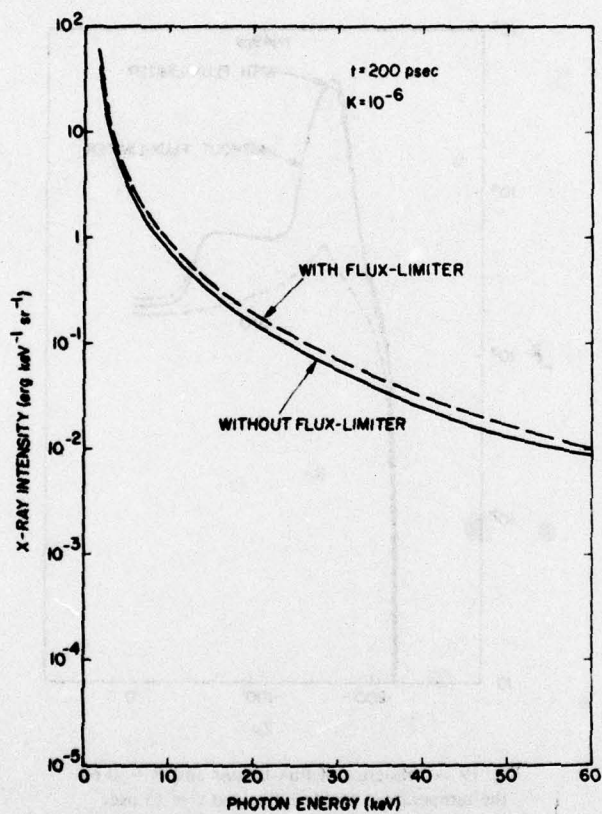


Fig. 20 — Influence of flux-limiter on X-ray spectra at $t = 200 \text{ psec}$ for $K = 10^{-6}$.